ADVANCED MATERIALS
www.advmat.de

Revisiting the Epitaxial Growth Mechanism of 2D TMDC Single Crystals

Chenyang Li, Fangyuan Zheng, Jiacheng Min, Ni Yang, Yu-Ming Chang, Haomin Liu, Yuxiang Zhang, Pengfei Yang, Qinze Yu, Yu Li, Zhengtang Luo, Areej Aljarb, Kaimin Shih, Jing-Kai Huang, Lain-Jong Li, and Yi Wan**

Epitaxial growth of 2D transition metal dichalcogenides (TMDCs) on sapphire substrates has been recognized as a pivotal method for producing wafer-scale single-crystal films. Both step-edges and symmetry of substrate surfaces have been proposed as controlling factors. However, the underlying fundamental still remains elusive. In this work, through the molybdenum disulfide (MoS_2) growth on C/M sapphire, it is demonstrated that controlling the sulfur evaporation rate is crucial for dictating the switch between atomic-edge guided epitaxy and van der Waals epitaxy. Low-concentration sulfur condition preserves O/Al-terminated step edges, fostering atomic-edge epitaxy, while high-concentration sulfur leads to S-terminated edges, preferring van der Waals epitaxy. These experiments reveal that on a 2 in. wafer, the van der Waals epitaxy mechanism achieves better control in MoS_2 alignment (≈99%) compared to the step edge mechanism (<85%). These findings shed light on the nuanced role of atomic-level thermodynamics in controlling nucleation modes of TMDCs, thereby providing a pathway for the precise fabrication of single-crystal 2D materials on a wafer scale.

1. Introduction

Transition metal dichalcogenides (TMDCs) represent a class of 2D semiconducting materials with considerable potential for next-generation electronic devices.[1] However, the realization of such applications necessitates the fabrication of wafer-scale single crystals.[2] From a theoretical standpoint, two primary methodologies have been proposed to achieve 2D TMDCs single crystal growth. The first is to control single nucleation followed by the continuous expansion of the grain size to attain wafer-scale single crystals.[3] Despite notable advancements, this method faces significant challenges, particularly when scaled to industrial requirements, such as the growing films on large wafers and the attainment of high-efficiency yields. Alternatively, the second approach entails the epitaxial

C. Li, F. Zheng, N. Yang, Y.-M. Chang, H. Liu, P. Yang, L.-J. Li, Y. Wan
Department of Mechanical Engineering
The University of Hong Kong
Hong Kong 999077, China
E-mail: lanceli1@hku.hk; wanyi@hku.hk

J. Min, K. Shih
Department of Civil Engineering
The University of Hong Kong
Hong Kong 999077, China

Y. Zhang
Department of Electrical and Electronic Engineering
The University of Hong Kong
Hong Kong 999077, China

Q. Yu, Y. Li
Department of Computer Science and Engineering
The Chinese University of Hong Kong
Hong Kong SAR 999077, China

The ORCID identification number(s) for the author(s) of this article can be found under https://doi.org/10.1002/adma.202404923

DOI: 10.1002/adma.202404923

Y. Li
The CUHK Shenzhen Research Institute
Hi-Tech Park
Nanshan, Shenzhen 518057, China

Z. Luo
Department of Chemical and Biological Engineering
The Hong Kong University of Science and Technology
Hong Kong 999077, China

A. Aljarb
Physical Sciences and Engineering Division
King Abdullah University of Science and Technology (KAUST)
Thuwal 23955-6900, Kingdom of Saudi Arabia

A. Aljarb
Department of Physics
King Abdulaziz University
Jeddah 21589, Kingdom of Saudi Arabia

J.-K. Huang
Department of Systems Engineering
City University of Hong Kong
Hong Kong 999077, China

growth of oriented multi-nucleation on a crystalline substrate, followed by their seamless integration into a wafer-scale single crystal. This technique has successfully produced various 2D single crystals at the wafer scale;[4] however, the mechanisms governing the control of crystal lateral orientation are still under active investigation and debate within the scientific community.

The creation of vicinal surfaces, rich in parallel step edges, has been established as an effective strategy for directing the orientation of 2D grains.[4c,5] These step edges on the substrate act as prime nucleation sites, initiating and guiding the 2D crystal's orientation towards uniformity. For example, Yang et al. have shown that single-oriented molybdenum disulfied (MoS_2) monolayers can be synthesized on vicinal Au (111) surfaces, facilitated by the preferential docking of a Mo-zz edge with atomic steps.[6] Similarly, Li et al. intentionally employed C/A axis miscut orientation to generate step edges along the M direction, overcoming the nucleation energy degeneracy for antiparallel domains, and successfully produced wafer-scale single-crystal MoS_2.[4d] This approach, known as atomic-edge guided epitaxy, is now widely recognized as the predominant mechanism for the growth of single-crystal TMDCs on gold and sapphire substrates.

Conversely, there are emerging discussions suggesting that van der Waals epitaxy—characterized by the weak van der Waals interactions between 2D grains and substrate surfaces—plays a crucial role in the deterministic control of single orientation growth on both gold[6,7] and sapphire substrates.[8] Statistical analyses of Molecular Beam Epitaxy (MBE) grown, single-oriented 2D TMDCs on Au(111) substrates reveal that over 88% of TMDC nucleation occurs on surface terraces,[7a] rather than docking at the step edges. Additionally, our recent investigations highlight the importance of refining single-exposed sapphire crystal surface slabs to achieve unidirectional nucleation on sapphire surface terraces, further underscoring the complexity of the growth mechanisms involved.[8e]

While both atomic-edge guided epitaxy and van der Waals epitaxy are theoretically sound and supported by robust experimental evidence, the precise factors underlying the growth mode still remain elusive. Notably, several research works have highlighted the pivotal role of growth conditions—particularly the ratio of metal to chalcogen precursors—in determining the orientation of 2D TMDCs during the epitaxial process. For example, Suenaga et al. have shown that the orientation of MoS_2 on c-plane sapphire can exhibit two distinct perpendicular directions, which can be manipulated by adjusting the sulfur concentration.[8d] Furthermore, various works on chemical vapor deposition (CVD)-grown, unidirectionally aligned TMDCs assert that a high chalcogen-to-metal ratio is crucial for obtaining wafer-scale single-crystal films.[4a,5f,6,7b,8b,d,9] Despite these findings, a comprehensive theoretical framework that convincingly elucidates the impact of precursor concentration on orientation control has yet to be developed at the atomic interaction level. This highlights a significant gap in the field, as experimental evidence that directly reflects these atomic interactions is still missing.

In this study, we utilized C towards M axis (C/M) sapphire substrates with a miscut angle ranging from 0.2° to 2° to explore the impact of precursor concentration on the epitaxial growth modes of 2D TMDCs. Our systematic experimental results, underscored by atomic-resolution cross-sectional scanning transmission electron microscopy (STEM) images, reveal that a low S/Mo ratio preserves the active oxygen (O)/aluminum (Al)-terminated atomic edges. This condition facilitates the MoS_2 grains following atomic edge epitaxy with 0°/60° alignment, referenced to the A axis [11$\bar{2}$0]. Conversely, a high S/Mo ratio leads to sulfur (S)-terminated atomic edges, hindering edge nucleation. In such an instance, the terrace/surface symmetry dictates the growth orientation through van der Waals epitaxy, resulting in 30°/90° alignment. Simulations corroborate the selective docking behavior of MoS_2 nuclei at O/Al-terminated atomic edges, while such behavior is absent at S-terminated atomic edges. Leveraging this insight, 2-inch wafer-scale single-oriented MoS_2 monolayers on C/M sapphires with uniform electrical properties have been successfully synthesized with 90° alignment—a feat previously deemed unachievable. Our findings highlight the critical role of atomic-level thermodynamics in manipulating the nucleation modes of 2D materials. The elucidated mechanism comprehensively explains the orientation control observed in prior studies involving precursor concentration and paves the way for the precise and controlled fabrication of single-crystal 2D materials.

2. Results and Discussion

A typical CVD method, utilizing molybdenum oxide (MoO_3) and sulfur (S) powder as precursors, was employed to investigate the orientation and growth mode of MoS_2 on C towards M axis miscut (C/M) sapphire substrates, as shown in Figure S1 (Supporting Information). The sulfur powder was positioned upstream, with its consumption rate controlled by a heating tape, ranging from 0.75 to 3.2 mg min^{-1}. The MoO_3 powder was placed upstream of the high-temperature heating furnace, featuring a consumption rate of 1.6 mg min^{-1}. C/M sapphire substrates were pretreated at high annealing temperatures between 1000 to 1300 °C in a muffle furnace to achieve uniform surfaces with atomic steps.[8e] After annealing, the sapphire substrates were placed downstream of the furnace. Figure S1 (Supporting Information) illustrates the set-up of the CVD system.

Figure 1a–c displays the distinct preferential growth orientations of MoS_2 monolayers on C/M 1° substrates, varying with the increase in sulfur evaporation rate from 0.9 to 3.2 mg min^{-1}. At a relatively low S evaporation amount, as depicted in Figure 1a and Figure S2a,b (Supporting Information), the edges of MoS_2 triangles, identified as the zigzag-S direction [11$\bar{2}$0], aligned parallel to the step direction, indicating a 0°/60° alignment. Intriguingly, with an increase in sulfur evaporation, a portion of the MoS_2 exhibited a 30°/90° orientation change, leading to mixed orientations, as illustrated in Figure 1b. Upon further increasing the sulfur evaporation amount, the dominant MoS_2 orientation transitioned to a 30°/90° alignment (Figure 1c and Figure S2c,d, Supporting Information). It has been reported that an insufficient-S condition can result in the formation of MoO_x seeds, leading to randomly oriented MoS_2 growth on untreated sapphire surfaces.[10] A similar phenomenon was also observed on our annealed substrates when the S evaporation rate was decreased to 0.8 mg min^{-1} (shown in Figure S3, Supporting Information).

Previous reports have demonstrated that MoS_2 on annealed C-plane sapphire prefers a 30°/90° rotation configuration, attributed to the van der Waals interactions.[2d,8d,11] However, when

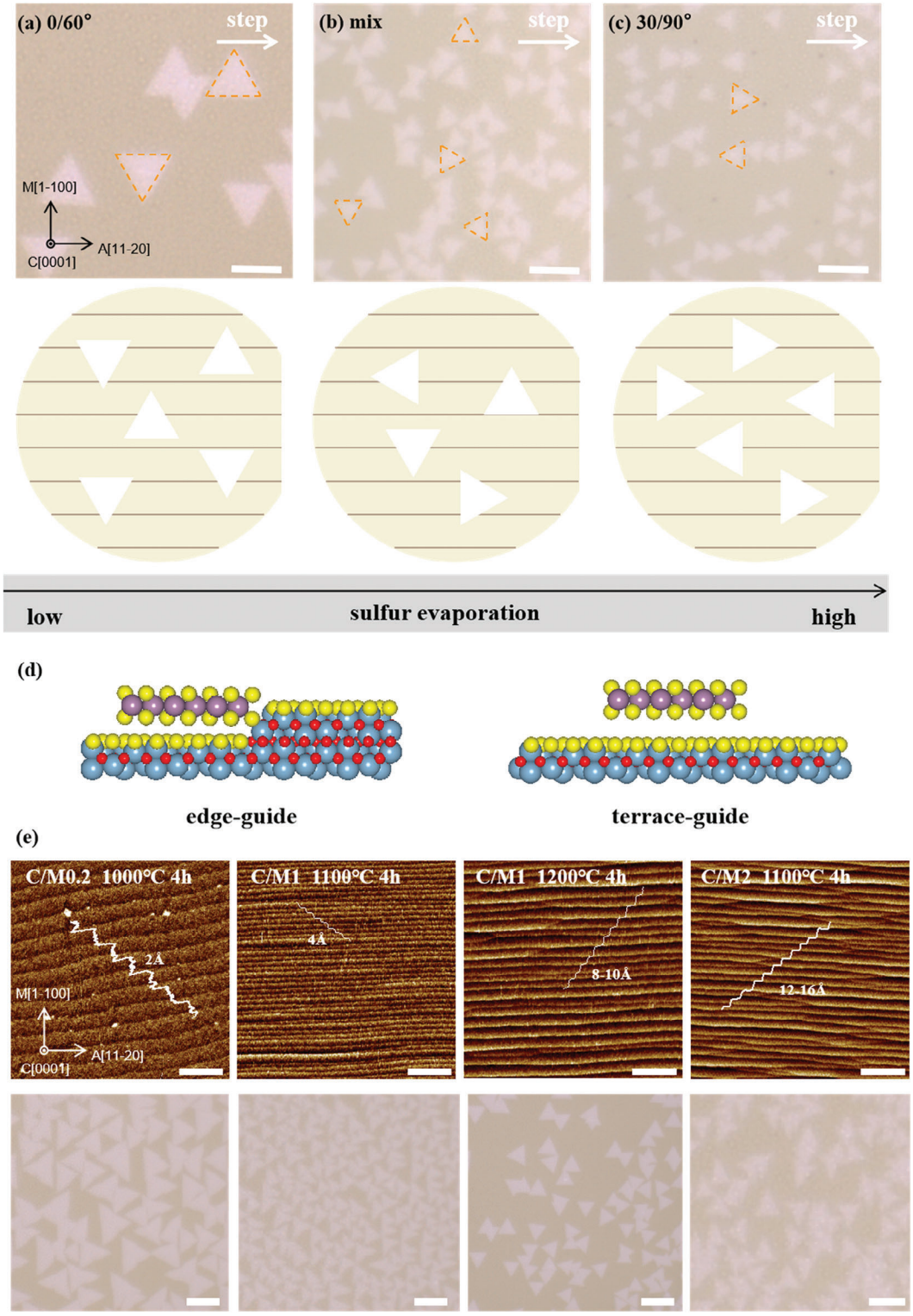

Figure 1. Variations in MoS_2 growth modes on C/M sapphire substrates. a–c) Optical microscopy (OM) and schematic images illustrating the impact of varying sulfur evaporation rates on MoS_2 growth orientations: a) at 0.9 mg min^{-1}, demonstrating a 0/60° alignment, b) at 1.5 mg min^{-1} showing mixed alignments, and c) at 2.3 mg min^{-1} revealing 30/90° alignment. d) Schematic illustrating the two primary mechanisms of epitaxial growth on sapphire substrates: atomic-edge guided epitaxy, facilitated by step edges, and van der Waals epitaxy, occurring on terraces. e) AFM images of annealed sapphire substrates featuring different step heights (scale bar: 200 nm), alongside corresponding OM images of MoS_2 grown under identical conditions with a S evaporation rate of 1.5 mg min^{-1}. (Scale bar: 5 µm).

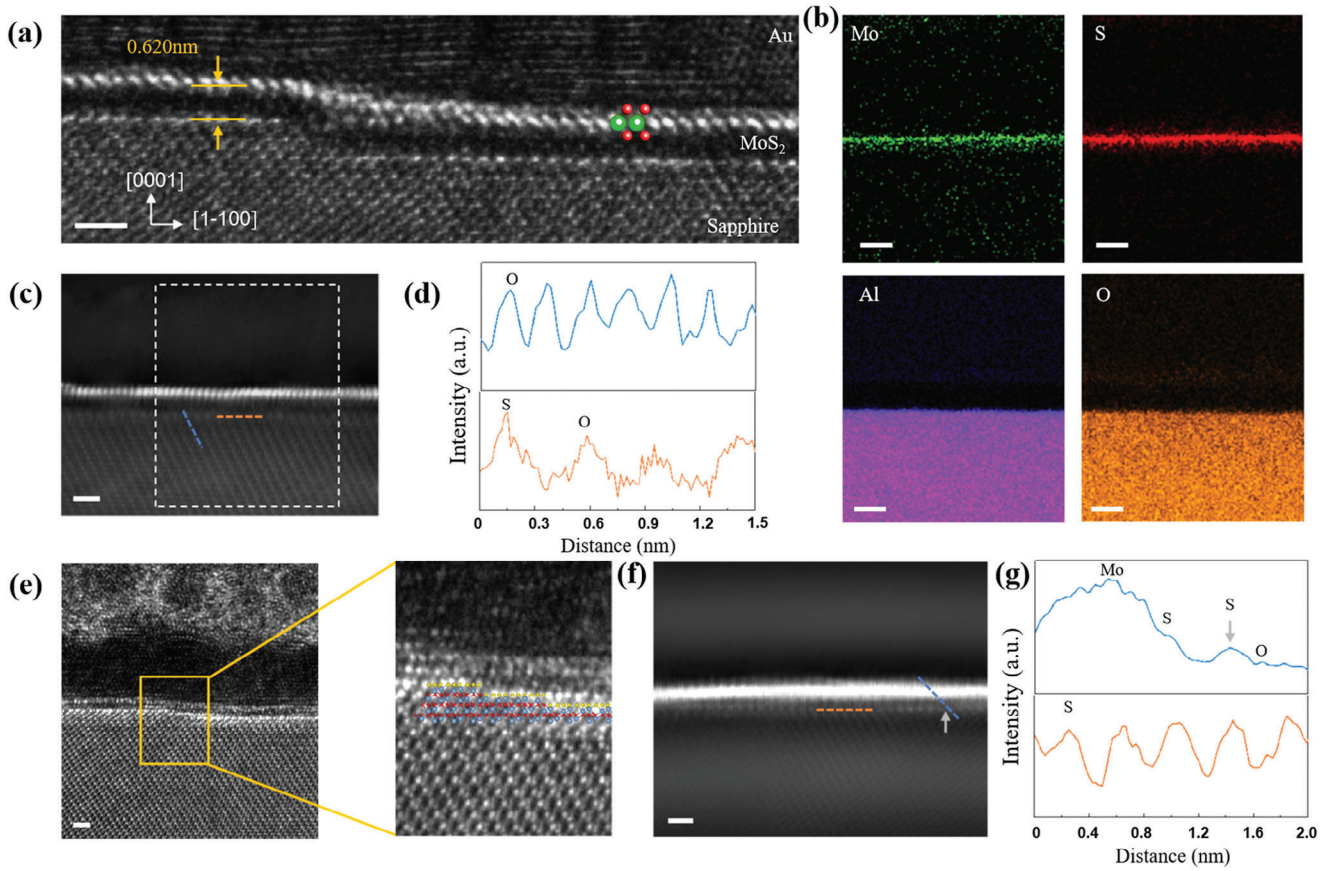

Figure 2. Surface reconstruction of C/M sapphire after MoS_2 growth. a) Cross-sectional HRTEM image of a monolayer MoS_2 on sapphire under low S/Mo ratio condition. b) STEM-EDS elemental mapping for Mo, S, Al, and O of the rectangle area in (c). c) Cross-sectional HAADF-STEM image of a monolayer MoS_2 on sapphire under low S/Mo ratio condition. d) Intensity profile along blue and orange dashed lines in (c). e) Cross-sectional HRTEM image of a monolayer MoS_2 on sapphire under high S/Mo ratio condition. f) Cross-section HAADF-STEM image of a monolayer MoS_2 on sapphire under high S/Mo ratio condition. g) Intensity profile along blue and orange dashed lines in (f). Scale bars in all images are 1 nm.

considering the strong bonding between the zigzag edges of MoS_2 and the atomic steps of C/M sapphire along [11$\bar{2}$0] direction, the preferred orientation of MoS_2 growth shifts toward a 0/60° alignment.[4d] It is worth noting that although step edges provide nucleation sites and directional guidance, the MoS_2 grains remain aligned along the [11$\bar{2}$0] direction of c-plane sapphire lattice regardless of the exact step angle.[5f,12] Consequently, as shown in Figure 1d, the epitaxial growth mode of MoS_2 on C/M sapphire substrates transitions from atomic-edge guided epitaxy to the van der Waals epitaxy with an increase in the sulfur evaporation rate.

It is crucial to highlight the significant role of the substrate's annealing process, as it generates uniform atomic steps, thereby facilitating the coexistence of two distinct growth modes. To delve deeper into how the structure and height of these steps influence the control over the epitaxy mode, we conducted systematic studies. Figure 1e presents AFM images showcasing well-aligned steps along the [11$\bar{2}$0] direction, attributed to the M-axis miscut angles. By adjusting both the miscut angle and annealing temperature, we were able to tailor step heights from 2 to 16 Å, as shown in Figure S4 (Supporting Information). Intriguingly, under identical growth conditions with the S evaporation rate of 1.5 mg min^{-1}, MoS_2 grown on substrates with low step heights exhibits a 30/90° alignment. Conversely, an increase in step height to 8–10 Å leads to mixed orientations, whereas step heights of 12–16 Å distinctly favor a 0°/60° alignment. This indicates that step height significantly influences growth mode control, with taller steps more effectively promoting atomic edge-guided epitaxial growth.

To elucidate the epitaxial relationship between MoS_2 and the substrate, we prepared cross-sectional samples of monolayer MoS_2 grown on sapphire under different S/Mo ratios. Figure S5 (Supporting Information) shows the cross-sectional fabrication process of a MoS_2 sample grown under a high S/Mo ratio. Samples with both a high S evaporation rate (aligned at 30/90°) and a low S evaporation rate (aligned at 0°/60°) were fabricated perpendicular to the step edge of sapphire using a focused ion beam (FIB). High-resolution transmission electron microscopy (HRTEM) image, as shown in **Figure 2a**, reveals MoS_2/Al_2O_3 interfaces under low S/Mo ratio conditions along Al_2O_3 [11$\bar{2}$0] direction. The Mo-to-Al distance is measured at 0.620 nm, indicative of an ideal van der Waals interface between MoS_2 and sapphire, which is further corroborated in Figure 2b from energy-dispersive X-ray spectroscopy (EDS) elemental mapping. Notably, high-angle annular dark-field scanning transmission electron microscopy (HAADF-STEM) intensity profiles display variations

in atomic contrast on the sapphire surface. A few O atoms in the topmost Al_2O_3 layer are substituted by S, yielding a higher contrast than the underlying O atoms, as shown in Figure 2c,d. These results suggest that a low S evaporation rate leads to only partial substitution of O atoms with S atoms, forming an O/S mixed interface, which is a key factor causing antiparallel growth of 2D materials on sapphire.[5f,8e]

The cross-sectional HRTEM image in Figure 2e shows the van der Waals interface between MoS_2 and sapphire under a high S/Mo condition. Conversely, as demonstrated in Figure 2f,g, all O atoms in the topmost Al_2O_3 layer are replaced by S with a high S evaporation rate, creating a uniformly S-passivated surface. A uniform interface is believed to be essential for single orientation epitaxy.[8d,13] To confirm the presence of S passivation, we conducted EDS mappings of both samples in the same selected area, including MoS_2 and sapphire surfaces. The S/Mo ratios were found to be 2.69 and 2.57 for high S/Mo (Figure S6a–d, Supporting Information) and low S/Mo (Figure S6e–h, Supporting Information) samples, respectively, suggesting a variation in the content of S dopants on sapphire. Interestingly, HAADF-STEM images reveal that under low S/Mo conditions, S atoms only partially replace O on the terrace and maintain an O/Al-terminated atomic edge (Figure S7a, Supporting Information). In contrast, under high S/Mo conditions, both the terrace and step edges are substituted by S atoms, as shown in Figure S7b (Supporting Information). This indicates that sulfur atoms preferentially replace O atoms on the sapphire terrace surfaces rather than at the step edges. Additionally, atomic images provide clear evidence for the 0°/60° alignment of MoS_2 at low S/Mo ratio, and the 30°/90° alignment when the ratio is high (Figure S8, Supporting Information).

Figure S9 (Supporting Information) presents the HAADF-STEM image of a higher step (8 Å) after MoS_2 growth under high S/Mo conditions (S evaporation rate of 1.5 mg min^{-1}), where the edge remains O/Al-terminated. Upon comparing step edges of varying heights under the same S/Mo ratio, it is evident that higher step edges exhibit a larger exposed surface area, rendering them more challenging to passivate with sulfur atoms relative to lower step edges. This incomplete passivation of higher steps facilitates MoS_2 nucleation guided by the step edges, thus elucidating the differing growth orientations of MoS_2 under consistent sulfur evaporation conditions as observed in Figure 1e.

Although the formation of a chalcogen passivation layer on the sapphire surface has been reported in several studies, few have offered atomic resolution images to elucidate the structure of this passivation layer, especially at the step edges. Our results demonstrate that an S-terminated atomic edge forms exclusively under high S/Mo conditions. This phenomenon is proposed as the key factor driving the transition in growth mode from atomic-edge epitaxy to van der Waals epitaxy.

Density functional theory (DFT) calculations were conducted using atomic models of sapphire step edges, constructed based on cross-sectional STEM images. Figure S10a,b (Supporting Information) depicts the atomic models for 0.4 nm O/Al-terminated and S-terminated sapphire steps, respectively. The key distinction between these two types of step edges is the passivation effect of sulfur atoms on the step sides. Specifically, the O/Al-terminated steps feature a sharp edge, with both O and Al atoms exposed, while the S-terminated steps present a stair-like configuration, being completely passivated by S atoms.

To assess the impact of atomic edges on nucleation, DFT calculations first simulated the interactions between MoS_2 and sapphire substrates with O/Al-terminated step edges. Following relaxation, the edge S atoms of MoS_2 nuclei formed strong bonds with exposed Al atoms at the sapphire step edges, as shown in **Figure 3**a. Compared to the terrace-induced nucleation illustrated in Figure 3b, the step-edge offers energetically favorable sites for adsorption, as demonstrated by the comparison of adsorption energies in Figure 3c. Moreover, orientation angle-dependent simulation results indicate that atomic edge-guided epitaxy could potentially direct single-oriented MoS_2 growth with 60° alignments.

However, experimental findings indicate challenges in achieving highly single-oriented MoS_2 growth with 0/60° alignment, with the best outcomes showing approximately 85% unidirectional growth, as demonstrated in Figure S11 (Supporting Information). This discrepancy can be attributed to: 1) the complexity of the edge structure, which may undergo partial substitution by S atoms during growth, leading to various atomic edge formations and consequently, antiparallel growth; and 2) the possibility of MoS_2 nucleation occurring at either the bottom or top of the steps, also resulting in antiparallel growth.[5f]

Conversely, when MoS_2 nuclei form on S-terminated sapphire steps, the simulation outcomes depicted in Figure 3d reveal a pronounced difference: no bond is formed between the MoS_2 nuclei and the step edges. This shift is largely due to the significantly reduced inductive effect exerted by the sulfur atoms of the fully passivated layer. Consequently, the S-terminated sapphire step edge exerts less influence on guiding MoS_2 nucleation. Instead, the interaction between MoS_2 and the sapphire terrace structure becomes crucial in directing the epitaxy process.

The distribution of adsorption energy as the MoS_2 flakes rotate from 0 to 120° on S-terminated step edges, illustrated in Figure 3e, indicates that the 90° orientation is the most energetically stable configuration for MoS_2 flakes on S-terminated step edges. These results are consistent with our previous simulations,[8e] which showed that MoS_2 on C-plane sapphire surfaces, following van der Waals epitaxy, tends to align at 90° on S-terminated sapphire surfaces. These findings are in strong agreement with our experimental observations.

In our previous work,[8e] we found that mirror-reflected sapphire surfaces exist when the step height is randomly distributed on commercialized sapphire, which induces antiparallel MoS_2 growth. Additionally, mixed O/S-terminated surface nucleation also leads to antiparallel growth. To facilitate the growth of single-crystal MoS_2, we meticulously annealed the sapphire substrates to achieve uniformly distributed, even-numbered steps,[8e] as shown in Figure S4d (Supporting Information). This preparation ensures a single-exposed atomic surface during the growth process. Leveraging a high S/Mo ratio to create S-terminated step edges and atomic surfaces enabled the attainment of wafer-scale MoS_2 single crystals on C/M sapphire via van der Waals epitaxy, as shown in **Figure** 4a. The uniformity performance of the 2 in. wafer MoS_2 film can be found in Figure S12 (Supporting Information).

It is worth noting that the C/M sapphire used in this work was previously considered unsuitable for single crystal MoS_2 growth in other research systems.[4d] This may be due to different

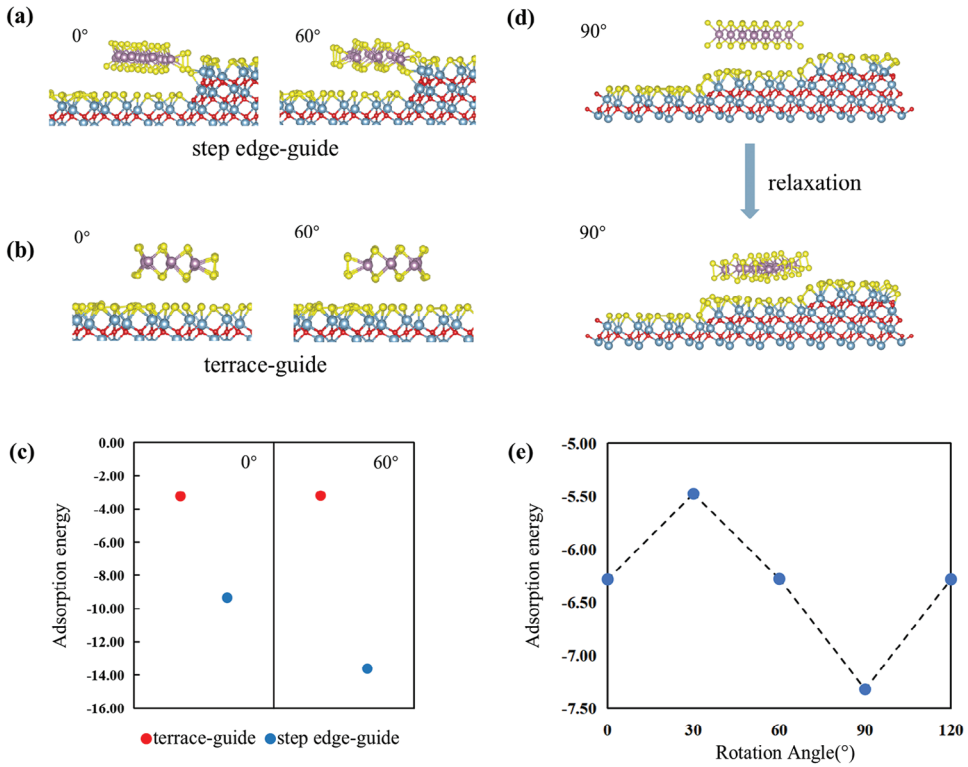

Figure 3. Mechanism of MoS_2 growth mode transition. Atomic schematic illustrating the relaxed structures of MoS_2 ribbons, rotated at 0° and 60°, a) situated less than 2.78Å from an O/Al-terminated step edge, demonstrating the atomic edge-guided growth; and b) positioned over 0.57 nm from the O/Al-terminated step, representing the terrace-guided growth. c) The adsorption energy distribution of MoS_2 rotating at 0° and 60° under conditions of step edge-guide growth (related to a) and terrace-guide growth (related to b). d) Initial and relaxed structure of MoS_2 flakes at 90° on S-terminated sapphire steps. e) The adsorption energy distribution of MoS_2 flakes rotating from 0° to 120° on S-terminated step edges.

atomic structures formed in varying reaction environments. For example, the introduction of Se,[5f,13a] O_2,[4d,13b] and H_2[14] as reaction gases can lead to different surface reactions, forming distinct atomic structures on terraces and steps. Additionally, other TMDCs grown on sapphire also exhibit different orientation preferences and even on the substrates with same crystal index, as shown in Table S1 (Supporting Information), suggesting that growth conditions modulate the surface structures and thus the growth behaviors. Therefore, to achieve reliable single-crystal growth, it is essential to investigate the atomic structure variations during growth and apply suitable growth conditions that ensure the desired nucleation mode.

Figure 4b showcases optical microscopy (OM) images of the unidirectionally aligned MoS_2 domains, with approximately 99.0% of these domains exhibiting a 90° alignment (statistics are provided in Figure S13, Supporting Information). The atomic force microscopy (AFM) image in Figure S14 (Supporting Information) confirms that the aligned MoS_2 edges are perpendicular to the direction of the sapphire step edges. Furthermore, the second harmonic generation (SHG) mapping presented in Figure 4b verifies that the MoS_2 monolayers are aligned, without the formation of grain boundaries between any two merged grains.

The Raman spectra (Figure S15a, Supporting Information) of MoS_2 flakes exhibit characteristic peaks corresponding to the $E_{2g}{}^1$ and A_{1g} modes of the MoS_2 lattice, with the frequencies indicating the thickness of the flakes as monolayer. The full width at half maximum (FWHM) of $E_{2g}{}^1$ and A_{1g} peaks is 3.46 and 4.76 cm^{-1}, respectively. The photoluminescence (PL) spectrum shown in Figure S15b (Supporting Information) further corroborates the high quality of the single-crystal MoS_2 in our study, as evidenced by the narrow full width at half maximum (FWHM), approximately 19 nm.

The field-effect transistor (FET) device array was fabricated based on our large-scale MoS_2 film (Figure 4c and Experimental Section). Figure 4d demonstrates the transfer curve and current distribution of 60 FET devices (randomly extracted from Figure 4c area) with a channel length of 1.5 μm (inset illustration of Figure 4d exhibits the device structure of the FET device). Attributed to the excellent uniformity of single crystal MoS_2, all selected FET devices exhibited normal operation with 18.3% variation in the on-state current (demonstrated as $SI_{on} / < I_{on} >$),[15] where SI_{on} and $< I_{on} >$ represent standard deviation and the mean value of the on current, respectively.) Notably, the output curve of the FET devices exhibits a linear current-voltage relation (Figure 4e), indicating good Ohmic contacts formed at the source and drain electrodes on the single-crystal MoS_2 film. Furthermore, Field-effect mobility and device on/off ratio were statistically analyzed for the 60 measured FET devices, both showing Gaussian distributions. The average and maximum field-effect mobility reached 35.9 and 45.09 $cm^2\ V^{-1}\ s^{-1}$, respectively, with a field-effect mobility variation of 9.14%. The devices also exhibited a high on/off ratio, with an average value exceeding 10^8,

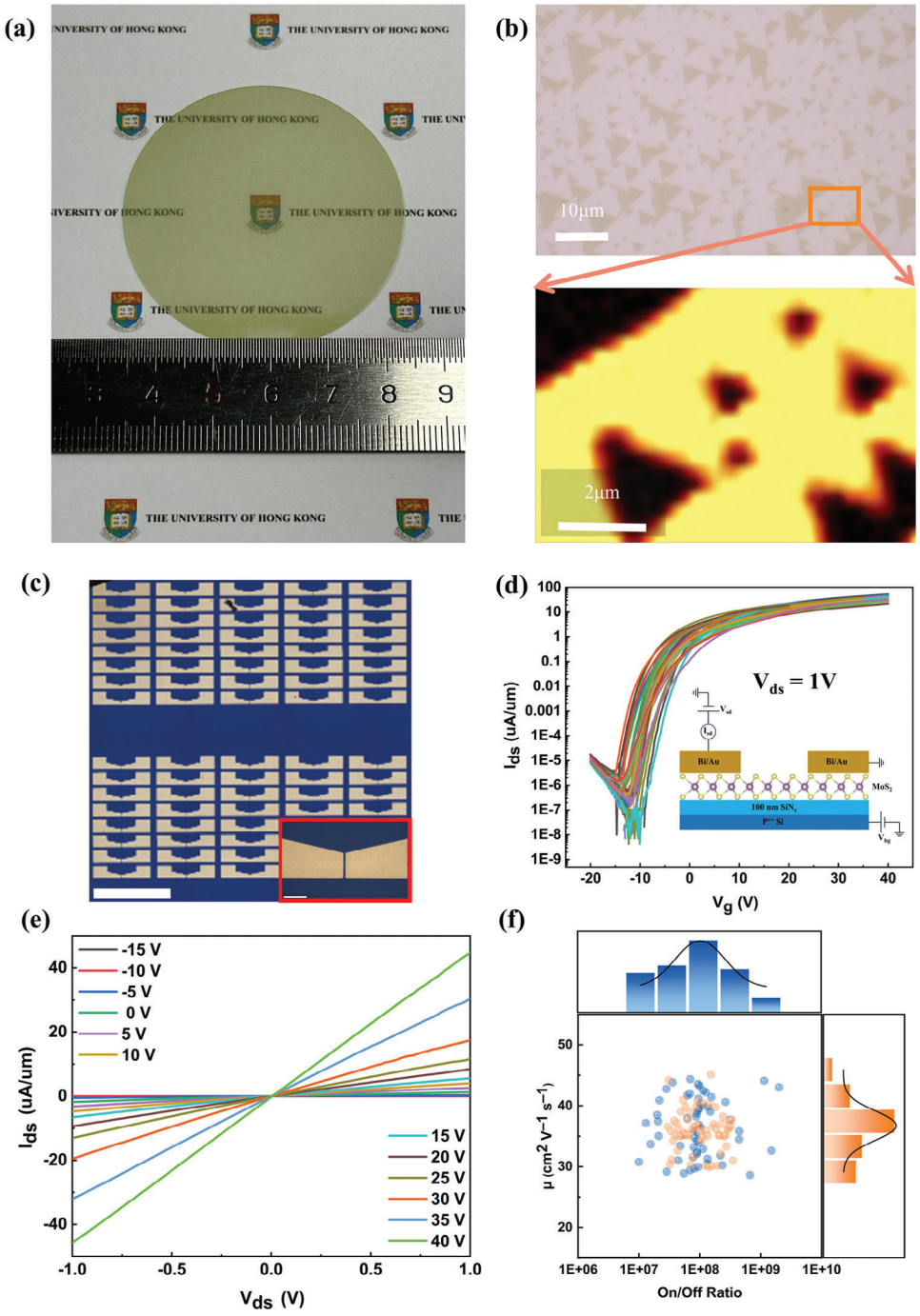

Figure 4. High-quality single-crystal MoS_2 growth on C/M 1° sapphire. a) Photograph of a 2 in. wafer scale single-crystal MoS_2 monolayers on C/M 1° sapphire. b) OM image of single orientation MoS_2 grains and corresponding polarized SHG mapping. c) OM image of a fabricated FET array. Scale bar: 1 mm. Inset: enlarged image of one FET device. Scale bar: 20 μm. d) Transfer characteristics of 60 MoS_2 FETs with a channel length of 1.5 μm. Inset: Illustration of the FET device structure. e) Output characteristics of the device in (d). From bottom to top, $V_{gs} = -15$ to 40 V with 5 V steps. f) Statistical distribution of field-effect mobility and FET devices on/off ratio. The field-effect mobility is extracted from the linear range of the transfer curve at V_{gs} = 20 V.

illustrated in Figure 4f. These results are comparable to the devices fabricated on the CVD MoS_2 films.[15,16]

3. Conclusions

In summary, we have demonstrated the critical role of sulfur evaporation rate in dictating the atomic edge structure of sapphire during the epitaxial growth of MoS_2. Specifically, there are two ways to grow single-oriented MoS_2 on sapphire. One approach is to control uniform Al/O step edges to ensure atomic-edge guided growth with a single 60° alignment. However, experimentally, we have not found a suitable condition to form these uniform atomic edges, with the best outcomes showing approximately 85% unidirectional growth. On the other hand, by meticulously controlling the step height to ensure a single-exposed atomic surface, we successfully synthesized 2 in. scale 99.0% single-crystal MoS_2 thin films via van der Waals epitaxy. Our findings not only advance the understanding of growth mechanisms for 2D materials but also open avenues for the scalable production of high-quality single-crystal thin films, pivotal for future applications in electronics and optoelectronics.

4. Experimental Section

Substrate Processing: C/M sapphire substrates (Crystalwise Technology Inc.) were utilized with different off-cut angles, including C/M 0.2°, 1°, and 2°, in accordance with the industrial standard. All the substrates got surface reconstruction by thermal annealing in a furnace (Muffle Furnace NBD-M1700) at temperatures ranging from 1000 °C to 1200 °C. This annealing process resulted in an orderly arrangement of steps on the surface, with the step height being determined by the specific off-cut angles of the substrates.

Growth of MoS_2 Monolayer: The growth of the MoS_2 monolayer was conducted using the traditional chemical vapor deposition (CVD) system with the presence of precursors and annealed substrates. Sulfur (Sigma-Aldrich, 99.5%) powder and molybdenum trioxide (MoO_3) (Sigma-Aldrich, 99.5%) powder were separately placed in the upstream and center zone of a 3 in. quartz tube. The center heating zone where MoS_2 and substrate were located, was maintained at a temperature of 700 °C. Additionally, a heating belt for sulfur, operating at temperatures ranging from 160 °C to 180 °C, was employed to control the evaporation rate of sulfur during the growth process. The sulfur evaporation in the reaction was measured by comparing its weight before and after the reaction. Prior to the reaction, the sulfur source was precisely weighed using a high-precision analytical balance. This initial weight was recorded. After the completion of the reaction, the sulfur source was allowed to cool to room temperature. The remaining sulfur was then weighed using the same analytical balance to obtain the final weight. The evaporation rate (mg min^{-1}) was calculated by dividing this weight difference by the total reaction time (minutes). To facilitate the transport of vaporized precursors to the center growth zone, an Ar carrier gas flow of 200 standard cubic centimeters per minute (sccm) at 35 Torr was utilized. The growth process typically required 5 min to obtain MoS_2 grains for observation, and 10 min to obtain full coverage films. After the growth, the system was naturally cooled to room temperature.

Characterization: For the characterization of MoS_2 and the substrates, various advanced techniques were employed. Optical microscope images were obtained using the WITec alpha300R system. AFM measurements were conducted with the Dimension Icon from Bruker, providing detailed imaging of MoS_2 and the substrate surfaces. For spectroscopic analysis, Raman, photoluminescence, and second harmonic generation spectra were acquired using the WITec alpha300R system equipped with laser sources of 488 and 1064 nm.

Cross-section transmission electron microscopy (TEM) samples were prepared using a dual beam Thermo Scientific Helios 5CX focused ion beam/scanning electron microscope (FIB/SEM) system. A JEM-ARM200F transmission electron microscope with a corrected electron optical systems (CEOS) probe spherical (Cs) aberration corrector was used, operating at 200 keV. The camera length of STEM was 120 mm, and the defocus was around −4 nm. During image acquisition, the high-angle annular dark field (HAADF) figures were captured at 19 µs per pixel and all images are 1024 × 1024 pixels.

FET Fabrication and Electric Measurement: The as-grown MoS_2 single crystal film was transferred to a 100 nm SiN_x/ highly doped Si substrate by PMMA-assisted method. After this, Bi/Au (20/40 nm) was deposited as the contact electrodes by using a thermal system. Electrical measurements were carried out with a semiconductor characterization system (Keysight B1500A) in a high vacuum (≈10^{-5} Torr) and dark environment at room temperature. The field-effect mobility was calculated based on the transfer curve according to the expression.

$$\mu = \frac{L \cdot \left(dI_{ds}/dV_{gs}\right)}{W \cdot C_{ox} \cdot V_{ds}} \quad (1)$$

where L and W represent channel length and width, respectively. C_{ox} is the gate capacitance of SiN_x, which can be calculated via (μ_o is the vacuum permittivity, and μ_r (≈7.9) and d (≈100 nm) are the dielectric constant and thickness of SiN_x, respectively.) The maximum carrier mobility value is extracted at the linear part of transconductance where the $V_{gs} = 22$ V.

DFT Calculation: In this research, the Vienna Ab initio Simulation Package (VASP) package[17] was employed to investigate atomic behaviors. The calculations were carried out using the generalized gradient approximation (GGA) level of the Perdew-Burke-Ernzerhof (PBE) exchange-correlation functional.[18] The electron-ion interactions were described by projector-augmented wave (PAW) pseudopotentials,[19] and the electronic wavefunctions were expanded through a plane-wave basis set. The energy cutoff for the plane-wave basis set was chosen as 400 eV. To simulate continuous band structures for approximating the Fermi-Dirac distribution function, the Gaussian smearing technique[20] with a broadening value of 0.05 eV was utilized to smooth the discrete energy levels. To account for van der Waals interactions, Grimme DFT-D3 dispersion correction without damping method[21] was incorporated. Due to computational resource limitations, the Brillouin zone was sampled by only Gamma point in accordance with a Γ-centered Monkhorst–Pack scheme.[22] The convergence criterion for the electronic self-consistency was set to 1×10^{-6} eV for achieving an accurate description of the electronic structure. For the ionic relaxation, the convergence criterion was specified as 0.02 eV $Å^{-1}$ to ensure the minimization of forces on each atom.

Supporting Information

Supporting Information is available from the Wiley Online Library or from the author.

Acknowledgements

Y.W. and L.J.L. acknowledge the support from the National Key R&D Project of China (2022YFB4400100) and the University of Hong Kong. Y.W. thanks the support from the Guangdong Natural Science Fund (2023A15150777). L.J.L. thanks the support from the Jockey Club Hong Kong to the JC STEM lab of 3DIC and the Research Grant of the Council of Hong Kong (CRS_PolyU502/22).

Conflict of Interest

The authors declare no conflict of interest.

Author Contributions

C.L., F.Z., and J.M. contributed equally to this work. Y.W. conceived the project. C.L. and Y.Z. synthesized the TMDs. C.L. carried out the Raman, photoluminescence, and SHG characterizations. F.Z. and Z.L. conducted the cross-sectional TEM characterizations and HAADF images analysis. J.M., Q.Y., Y.L., and K.S. performed the first-principles calculations. C.L., Y.-M.C., and H.L. deal with annealing sapphire substrates and AFM scan. N.Y. and J.-K.H accomplished the fabrication and electrical characterization of MoS_2 FETs. C.L., F.Z., J.M., N.Y., Y.W., and L.-J.L. wrote the paper. All the authors provide valuable suggestions.

Data Availability Statement

The data that support the findings of this study are available from the corresponding author upon reasonable request.

Keywords

chemical vapor deposition, molybdenum disulfide, orientation control, sapphire substrate, surface reconstruction

Received: April 5, 2024
Revised: July 1, 2024
Published online: August 16, 2024

[1] a) Y. Wan, J. H. Fu, C. P. Chuu, V. Tung, Y. Shi, L. J. Li, *Chem. Soc. Rev.* **2022**, *51*, 803; b) M.-Y. Li, S.-K. Su, H. S. P. Wong, L.-J. Li, *Nature* **2019**, *567*, 169; c) C. J. Liu, Y. Wan, L. J. Li, C. P. Lin, T. H. Hou, Z. Y. Huang, V. P. H. Hu, *Adv. Mater.* **2022**, *34*, 2107894.

[2] a) Y.-H. Lee, X.-Q. Zhang, W. Zhang, M.-T. Chang, C.-T. Lin, K.-D. Chang, Y.-C. Yu, J. T.-W. Wang, C.-S. Chang, L.-J. Li, *Adv. Mater.* **2012**, *24*, 2320; b) Q. Wang, N. Li, J. Tang, J. Zhu, Q. Zhang, Q. Jia, Y. Lu, Z. Wei, H. Yu, Y. Zhao, *Nano Lett.* **2020**, *20*, 7193; c) X. Xu, T. Guo, H. Kim, M. K. Hota, R. S. Alsaadi, M. Lanza, X. Zhang, H. N. Alshareef, *Adv. Mater.* **2022**, *34*, 2108258; d) M. Chubarov, T. H. Choudhury, D. R. Hickey, S. Bachu, T. Zhang, A. Sebastian, A. Bansal, H. Zhu, N. Trainor, S. Das, *ACS Nano* **2021**, *15*, 2532; e) P. Yang, F. Liu, X. Li, J. Hu, F. Zhou, L. Zhu, Q. Chen, P. Gao, Y. Zhang, *Small Methods* **2023**, *7*, 2300165.

[3] a) K. S. Kim, D. Lee, C. S. Chang, S. Seo, Y. Hu, S. Cha, H. Kim, J. Shin, J.-H. Lee, S. Lee, *Nature* **2023**, *614*, 88; b) X. Xu, Y. Pan, S. Liu, B. Han, P. Gu, S. Li, W. Xu, Y. Peng, Z. Han, J. Chen, *Science* **2021**, *372*, 195; c) I. V. Vlassiouk, Y. Stehle, P. R. Pudasaini, R. R. Unocic, P. D. Rack, A. P. Baddorf, I. N. Ivanov, N. V. Lavrik, F. List, N. Gupta, *Nat. Mater.* **2018**, *17*, 318.

[4] a) P. Yang, D. Wang, X. Zhao, W. Quan, Q. Jiang, X. Li, B. Tang, J. Hu, L. Zhu, S. Pan, *Nat. Commun.* **2022**, *13*, 3238; b) H. Yu, M. Liao, W. Zhao, G. Liu, X. J. Zhou, Z. Wei, X. Xu, K. Liu, Z. Hu, K. Deng, *ACS Nano* **2017**, *11*, 12001; c) T.-A. Chen, C.-P. Chuu, C.-C. Tseng, C.-K. Wen, H. S. P. Wong, S. Pan, R. Li, T.-A. Chao, W.-C. Chueh, Y. Zhang, *Nature* **2020**, *579*, 219; d) T. Li, W. Guo, L. Ma, W. Li, Z. Yu, Z. Han, S. Gao, L. Liu, D. Fan, Z. Wang, Y. Yang, W. Lin, Z. Luo, X. Chen, N. Dai, X. Tu, D. Pan, Y. Yao, P. Wang, Y. Nie, J. Wang, Y. Shi, X. Wang, *Nat. Nanotechnol.* **2021**, *16*, 1201.

[5] a) T. Li, W. Guo, L. Ma, W. Li, Z. Yu, Z. Han, S. Gao, L. Liu, D. Fan, Z. Wang, *Nat. Nanotechnol.* **2021**, *16*, 1201; b) J. Wang, X. Xu, T. Cheng, L. Gu, R. Qiao, Z. Liang, D. Ding, H. Hong, P. Zheng, Z. Zhang, *Nat. Nanotechnol.* **2022**, *17*, 33; c) L. Chen, B. Liu, M. Ge, Y. Ma, A. N. Abbas, C. Zhou, *ACS Nano* **2015**, *9*, 8368; d) S. H. Choi, H. J. Kim, B. Song, Y. I. Kim, G. Han, H. T. T. Nguyen, H. Ko, S. Boandoh, J. H. Choi, C. S. Oh, *Adv. Mater.* **2021**, *33*, 2006601; e) L. Wang, X. Xu, L. Zhang, R. Qiao, M. Wu, Z. Wang, S. Zhang, J. Liang, Z. Zhang, Z. Zhang, *Nature* **2019**, *570*, 91; f) H. Zhu, N. Nayir, T. H. Choudhury, A. Bansal, B. Huet, K. Zhang, A. A. Puretzky, S. Bachu, K. York, T. V. Mc Knight, *Nat. Nanotechnol.* **2023**, *18*, 1295; g) L. Liu, T. Li, L. Ma, W. Li, S. Gao, W. Sun, R. Dong, X. Zou, D. Fan, L. Shao, *Nature* **2022**, *605*, 69.

[6] P. Yang, S. Zhang, S. Pan, B. Tang, Y. Liang, X. Zhao, Z. Zhang, J. Shi, Y. Huan, Y. Shi, *ACS Nano* **2020**, *14*, 5036.

[7] a) D. Ding, S. Wang, Y. Xia, P. Li, D. He, J. Zhang, S. Zhao, G. Yu, Y. Zheng, Y. Cheng, *ACS Nano* **2022**, *16*, 17356; b) Y. Xia, D. Ding, K. Xiao, J. Zhang, S. Xu, D. He, X. Yue, Q. Rao, X. Wang, S. Ding, *Nat. Sci.* **2023**, *3*, 20220059.

[8] a) D. Dumcenco, D. Ovchinnikov, K. Marinov, P. Lazic, M. Gibertini, N. Marzari, O. L. Sanchez, Y.-C. Kung, D. Krasnozhon, M.-W. Chen, *ACS Nano* **2015**, *9*, 4611; b) A. Aljarb, Z. Cao, H.-L. Tang, J.-K. Huang, M. Li, W. Hu, L. Cavallo, L.-J. Li, *ACS Nano* **2017**, *11*, 9215; c) J. Dong, L. Zhang, X. Dai, F. Ding, *Nat. Commun.* **2020**, *11*, 5862; d) K. Suenaga, H. G. Ji, Y.-C. Lin, T. Vincent, M. Maruyama, A. S. Aji, Y. Shiratsuchi, D. Ding, K. Kawahara, S. Okada, *ACS Nano* **2018**, *12*, 10032; e) J. H. Fu, J. Min, C. K. Chang, C. C. Tseng, Q. Wang, H. Sugisaki, C. Li, Y. M. Chang, I. Alnami, W. R. Syong, C. Lin, F. Fang, L. Zhao, T. H. Lo, C. S. Lai, W. S. Chiu, Z. S. Jian, W. H. Chang, Y. J. Lu, K. Shih, L. J. Li, Y. Wan, Y. Shi, V. Tung, *Nat. Nanotechnol.* **2023**, *18*, 1289.

[9] a) A. Cohen, P. K. Mohapatra, S. Hettler, A. Patsha, K. Narayanachari, P. Shekhter, J. Cavin, J. M. Rondinelli, M. Bedzyk, O. Dieguez, R. Arenal, A. Ismach, *ACS Nano* **2023**, *17*, 5399; b) A. Aljarb, J. Min, M. Hakami, J.-H. Fu, R. Albaridy, Y. Wan, S. Lopatin, D. Kaltsas, D. Naphade, E. Yengel, *ACS Nano* **2023**, *17*, 10010.

[10] D. Zhou, H. Shu, C. Hu, L. Jiang, P. Liang, X. Chen, *Cryst. Growth Des.* **2018**, *18*, 1012.

[11] Q. Ji, M. Kan, Y. Zhang, Y. Guo, D. Ma, J. Shi, Q. Sun, Q. Chen, Y. Zhang, Z. Liu, *Nano Lett.* **2015**, *15*, 198.

[12] P. Zheng, W. Wei, Z. Liang, B. Qin, J. Tian, J. Wang, R. Qiao, Y. Ren, J. Chen, C. Huang, X. Zhou, G. Zhang, Z. Tang, D. Yu, F. Ding, K. Liu, X. Xu, *Nat. Commun.* **2023**, *14*, 592.

[13] a) Y.-C. Lin, B. Jariwala, B. M. Bersch, K. Xu, Y. Nie, B. Wang, S. M. Eichfeld, X. Zhang, T. H. Choudhury, Y. Pan, *ACS Nano* **2018**, *12*, 965; b) L. Li, Q. Wang, F. Wu, Q. Xu, J. Tian, Z. Huang, Q. Wang, X. Zhao, Q. Zhang, Q. Fan, *Nat. Commun.* **2024**, *15*, 1825.

[14] a) H. G. Ji, Y.-C. Lin, K. Nagashio, M. Maruyama, P. Solís-Fernández, A. Sukma Aji, V. Panchal, S. Okada, K. Suenaga, H. Ago, *Chem. Mater.* **2018**, *30*, 403; b) Y. Hwang, N. Shin, *Nanoscale* **2019**, *11*, 7701.

[15] K. K. H. Smithe, S. V. Suryavanshi, M. Munoz Rojo, A. D. Tedjarati, E. Pop, *ACS Nano* **2017**, *11*, 8456.

[16] a) P.-C. Shen, C. Su, Y. Lin, A.-S. Chou, C.-C. Cheng, J.-H. Park, M.-H. Chiu, A.-Y. Lu, H.-L. Tang, M. M. Tavakoli, *Nature* **2021**, *593*, 211; b) J.-K. Huang, Y. Wan, J. Shi, J. Zhang, Z. Wang, W. Wang, N. Yang, Y. Liu, C.-H. Lin, X. Guan, *Nature* **2022**, *605*, 262.

[17] G. Kresse, J. Furthmüller, *Phys. Rev. B.* **1996**, *54*, 11169.

[18] J. P. Perdew, K. Burke, M. Ernzerhof, *Phys. Rev. Lett.* **1996**, *77*, 3865.

[19] G. Kresse, D. Joubert, *Phys. Rev. B.* **1999**, *59*, 1758.

[20] M. Methfessel, A. T. Paxton, *Phys. Rev. B.* **1989**, *40*, 3616.

[21] S. Grimme, *J. Comput. Chem.* **2006**, *27*, 1787.

[22] H. J. Monkhorst, J. D. Pack, *Phys. Rev. B.* **1976**, *13*, 5188.